SCIENCE CHINA
Chemistry

•ARTICLES•

https://doi.org/10.1007/s11426-024-2233-7

The secret of the magic gourd(I): biomass from various organizations of ourds as a sustainable source for high-performance supercapacitors

Shaoqing Zhang[1,2*], Xuchun Wang[2], Tianming Lv[3], Baixue Dong[4], Jiqi Zheng[5], Yang Mu[5], Miao Cui[6*], Ting Zhang[1] & Changgong Meng[5,6*]

[1]*College of Chemistry and Materials Engineering, Anhui Science and Technology University, Bengbu 233000, China;*
[2]*Anhui Province Quartz Sand Purification and Photovoltaic Glass Engineering Research Center, Anhui Science and Technology University, Bengbu 233000, China;*
[3]*Instrumental Analysis Center, Dalian University of Technology, Dalian 116024, China;*
[4]*School of Chemical Engineering, Zhejiang University of Technology, Hangzhou 310014, China;*
[5]*College of Environment and Chemical Engineering, Dalian University, Dalian 116622, China;*
[6]*School of Chemical Engineering, Dalian University of Technology, Dalian 116024, China*

Received July 2, 2024; accepted July 30, 2024; published online September 2, 2024

The classic cartoon "Calabash Brothers" describes a story of seven brothers born from a magic gourd uniting to defeat powerful enemies. In order to explore the secret of the magic gourd, several transition metals were used to synthesize metal silicates (C-MSi) by planted gourd leaves (GLs) and then the C-MSi materials were used to fabricate supercapacitor electrodes and devices with superior electrochemical performance. By integrating theoretical calculations and experimental results, the supercapacitor electrodes and devices obtained from the combination of transition metals with amorphous carbon exhibit superior electrochemical performance. In detail, in the three-electrode system, the NaOH etched materials (C-MSi) exhibited better electrochemical performance (for instance, as for C-CdSi, 607 F g^{-1} at 0.5 A g^{-1} and the capacitance retention of 98.2% after 10,000 cycles) than the unetched ones (i-C-MSi). Hybrid supercapacitor (HSC) devices also achieve very excellent electrochemical properties. Take C-CdSi//AC as an example, the areal specific capacitance with 691 mF cm^{-2} at 2 mA cm^{-2}, the energy density with 5.04 Wh m^{-2} at the power density of 22.2 W m^{-2} and the cycle stability with 87.3% after 6,000 cycles. This approach is very versatile and was also applied to produce many hierarchically structured metal-silicate materials of other biomass precursors, including roots, vines, flowers, fruits and seeds of the planted gourds. Thus, it is a potential way to prepare transition metal silicates using biomaterials for the enhancement of electrochemical performance and improvement of energy storage and conversion. Also, this paper preliminarily reveals the secret of the magic gourd.

gourd leave, alkali etching, metal silicates, supercapacitor, electrochemical performance

Citation: Zhang S, Wang X, Lv T, Dong B, Zheng J, Mu Y, Cui M, Zhang T, Meng C. The secret of the magic gourd(I): biomass from various organizations of ourds as a sustainable source for high-performance supercapacitors. *Sci China Chem*, 2024, 67, https://doi.org/10.1007/s11426-024-2233-7

1 Introduction

Calabash Brothers is a classic Chinese cartoon. In this story, seven different-colored gourds fall from their vine and magically transform into brothers with different personalities. They defeat powerful enemies through their own superpowers and cooperation. The seven brothers wore clothes of different colors: red, orange, yellow, green, cyan, blue and purple, which corresponded to their superpowers: infinite

*Corresponding authors (email: zhangsq@ahstu.edu.cn; mcui@dlut.edu.cn; cgmeng@dlut.edu.cn)

strength, thousand-mile eye and wind-accompanying ear, invulnerability, fire spraying, water spitting, invisibility, magic gourd, respectively. When they combine and become the Vajra Calabash, he owns all the superpowers and is hard to be defeated [1]. So, why do the Calabash Brothers own such superpowers?

Of course, we know that this cartoon was adapted from a mythological story rather than a real-life existence. However, this issue should be discussed from a scientific perspective, and energy storage and conversion can be used as a point of penetration. The generation and storage of electrical energy can offer great potential to satisfy the continuous energy demand and needs of the Calabash Brothers in the process of defeating enemies. This requires energy storage devices that can be easily retracted and released during the battle with the enemies. Supercapacitors (SCs) are the most likely devices to solve this problem, as they have the following characteristics: excellent power density and long cycle life [2,3]. What's more, in our opinion, the generation of these superpowers is related to their hidden nature, such as the elements and compounds contained in the leaves or other biomass precursors from the planted gourds. Carbon, silicon and oxygen are the most abundant elements in the biomass precursors from the planted gourds and they play an important role in the preparation and operation of SCs [4–8]. Nowadays, silicon-based bioderived carbons have been attracting enormous research interest in preparing electrode materials [9–12]. Compared with unsustainable carbon resources, silicon-based bioderived carbons can be prepared from renewable resources, especially biomass materials, for the applications of electrochemical energy storage [13–18]. These biomass materials include green algaes [19,20], bamboo leaves [21,22], grasses [23], kelps [24] and reed leaves [25,26], and it can even be extended to almost all plants. Like most biomass materials, the biomass precursors from planted gourds, including roots, vines, leaves, flowers, fruits and seeds have large specific surface areas and large amounts of carbon, silicon and oxygen and some small amounts of heteroatoms (nitrogen, phosphorus and sulfur, *etc*.). Carbonized biomass precursors from planted gourds with a 3D interconnected nanofibrous network microstructure have desired constituents with relatively high carbon content, ranging from approximately 53% to 87%. Therefore, they are suitable precursors for fabricating 3D silicon-based bioderived carbons [12]. So, in this regard, the biomass precursors from planted gourds can be used to prepare electrode materials for SCs. Research on the preparation of SCs with biomass precursors from planted gourds may become a good starting point for us to study the truth about magic gourds.

Herein, a scalable strategy is presented to fabricate hierarchical silicon-based bioderived carbons from natural gourd at 600 °C under a nitrogen atmosphere. Traces of nitrogen also take part in generating pores and serves as a doping element. Then, an HCl solution is used to remove metal oxides and carbonates from the carbonized biomass precursors and a non-toxic NaCl solution is employed as the activation media to increase the pore size. As a result, the as-obtained silicon-based bioderived carbons exhibit abundant multilevel hierarchical pores. Afterwards, various transition metals (Cd, Zn, Mn, Ni, Co, Fe and Cu) and the silicon-based bioderived carbons undergo hydrothermal reactions to obtain TMSs derived from carbons. Lastly, NaOH solution is used to remove the unreacted SiO_2 to obtain the final materials C-MSi (M = Cd, Zn, Mn, Ni, Co, Fe and Cu) [27–32]. In regard to these materials, the 3D network structure promotes rapid charge transfer [33], the multilevel hierarchical pores advantage the accessibility of the electrolyte to the electrode surface [34], the large specific surface area dedicates substantial active sites for charge capacity [35], the rich N (and P, S) doping introduces pseudo-capacitance and the TMSs derived on carbons provide redox reaction during the charging and discharging process [36]. Therefore, when adopted as electrode materials for SCs, metal-silicate electrodes and hybrid supercapacitor devices exhibit excellent electrochemical performance. This study provides an effective strategy to prepare supercapacitors with outstanding electrochemical properties and also provides a reasonable explanation for the superpowers of the Calabash Brothers.

2 Experimental

2.1 Materials

All analytical reagents including transition metal acetates ($Cd(OAc)_2{\cdot}2H_2O$, $Zn(OAc)_2{\cdot}2H_2O$, $Mn(OAc)_2{\cdot}4H_2O$, $Ni(OAc)_2{\cdot}4H_2O$, $Co(OAc)_2{\cdot}4H_2O$, $Fe(OAc)_2{\cdot}H_2O$ and $Cu(OAc)_2{\cdot}H_2O$), hydrochloric acid aqueous solution (HCl), sodium chloride (NaCl), sodium hydroxide (NaOH), active carbon (AC), poly(vinylidene difluoride) (PVDF), *N*-methyl-2-pyrrolidone (NMP) and ethanol are used directly without pretreatment and the source and purity of all chemicals used are specified in Supplementary material. Fresh roots, vines, leaves, flowers, fruits and seeds of the planted gourds were picked from farmland in Bengbu City, China. In this article, the main research content is to prepare supercapacitors using gourd leaves (GLs) as raw materials.

2.2 Synthesis of metal silicates

Figure 1 shows the schematic illustration of the preparation strategy of the metal silicates using gourd leaves (GLs) and Cadmium ion as an example. The first step is the preparation of C-SiO_2. In detail, the fragmented GLs were heated at 600 °C for 2 h in a nitrogen atmosphere to carbonize and then stirred in the 0.5 M HCl and 1.0 M NaCl solutions for

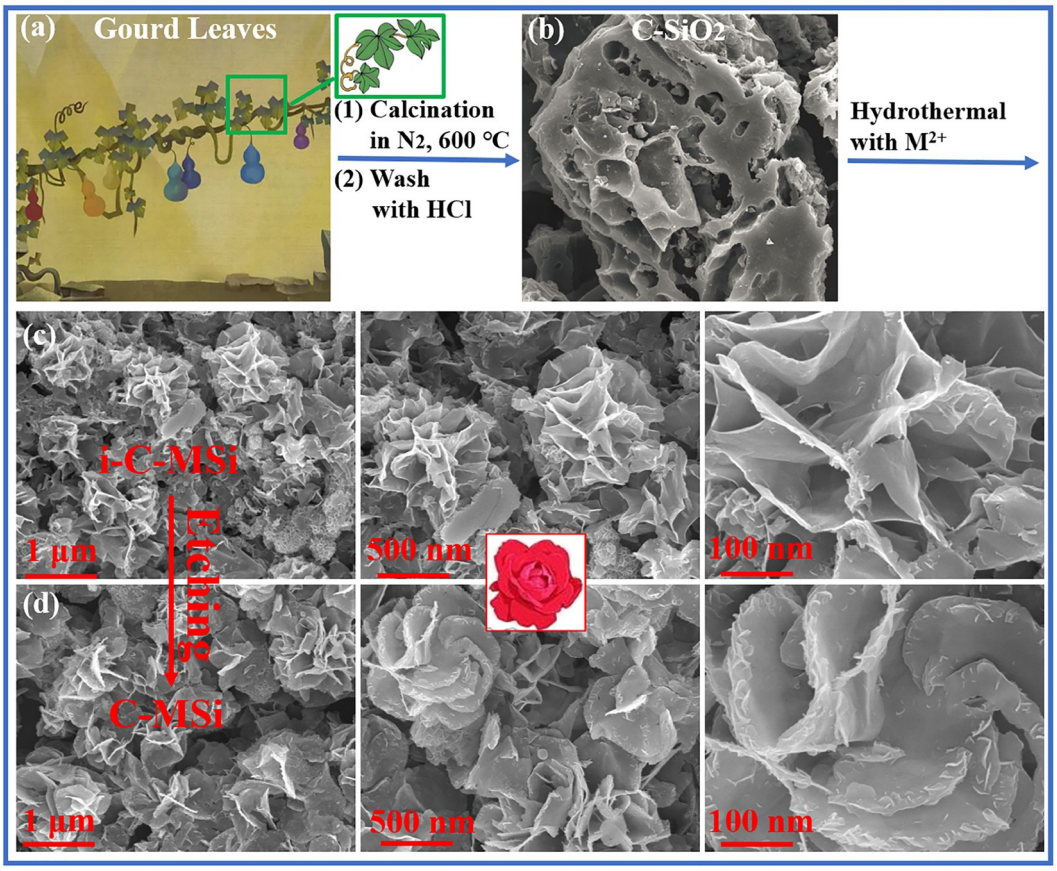

Figure 1 (Color online) Schematic illustration of the synthetic strategy of the i-C-MSi and C-MSi and their corresponding FE-SEM images: (c) i-C-MSi and (d) C-MSi (M = Cd, Zn, Mn, Ni, Co, Fe and Cu).

24 h to remove the impurities and increase the pore size. Then, C-SiO_2 was obtained, and according to the inductively coupled plasma-atomic emission spectroscopy (ICP-AES) measurement, the SiO_2 content was 15.31%. This is a step to obtain silicon-based bioderived carbons that exhibit abundant hierarchical pores. The second step is the synthesis of initial products with different ratios. Specifically, a certain amount of $Cd(OAc)_2{\cdot}2H_2O$ (0.0204, 0.0408, 0.0816, 0.1632 and 0.3264 g, corresponding to the Cd/Si molar ratios of 0.25/1, 0.5/1, 1/1, 2/1 and 4/1, respectively) was dispersed in 60 mL H_2O, then 0.12 g C-SiO_2 was added slowly under magnetic stirring. After stirring evenly, the colloids were heated at 180 °C for 24 h, then the i-C-CdSi-*x* (*x* = 1, 2, 3, 4 and 5) were synthesized. The final step is the alkali etching process. In particular, the i-C-CdSi-*x* materials were placed in a 3.0 M NaOH solution and stirred for 12 h. Then, the unreacted SiO_2 was etched off, and the final products were obtained (denoted C-CdSi-*x*). Based on the results of electrochemical testing, C-CdSi-3 exhibits the best electrochemical performance. Therefore, in this paper, C-CdSi-3 was mainly investigated. For ease of reading, we use C-CdSi instead of C-CdSi-3. Similarly, other transition metals (Zn^{2+}, Mn^{2+}, Ni^{2+}, Co^{2+}, Fe^{2+} and Cu^{2+}) were also used to synthesize metal silicates with different M/Si molar ratios and termed as C-ZnSi (Zn/Si = 1.5), C-MnSi (Mn/Si = 1.0), C-NiSi (Ni/Si = 1.5), C-CoSi (Co/Si = 1.5), C-FeSi (Fe/Si = 0.75) and C-CuSi (Cu/Si = 1.0), respectively. The synthetic procedures of other hierarchically porous metal-silicate derived from carbon materials are similar to the above materials except for using different biomass precursors (roots, vines, flowers, fruits and seeds) from the planted gourds.

2.3 Materials characterizations and electrochemical characterizations

The materials characterizations include ICP-AES, field emission scanning electron microscopy (FE-SEM), transmission electron microscopy (TEM), energy-dispersive X-ray spectrometer (EDS), X-ray powder diffraction (XRD), Fourier transform infrared spectroscopy (FTIR), Raman spectra, Brunauer-Emmett-Teller (BET), and X-ray photoelectron spectroscopy (XPS). The electrochemical properties of the as-obtained metal silicates are evaluated by assembling working electrodes and devices. As for the electrodes and devices of supercapacitors, the electrochemical characterizations include cyclic voltammetry (CV), galvanostatic charge/discharge (GCD) and electrochemical impedance spectroscopy (EIS) by using an electrochemical workstation

(CHI 660E). All detailed information is shown in Supporting Information online.

2.4 Calculation methods

All density functional theory (DFT) calculations in this work were performed with the Cambridge Serial Total Energy Package (CASTEP) code and Dmol 3 code on the basis of the revised Perdew-BurkeErnzerhof (RPBE) function, generalized gradient approximation (GGA) and the projector augmented wave (PAW) method. Calculation content and details can be found in Supporting Information online.

3 Results and discussion

3.1 Morphology, structure and composition of metal silicates

Figure 1 is the schematic illustration of preparing i-C-MSi and C-MSi (M = Cd, Zn, Mn, Ni, Co, Fe and Cu) from GLs. The i-C-MSi samples are synthesized as M^{2+} and SiO_2 reacted on the surface of C-SiO_2 after hydrothermal process at 180 °C for 24 h. The final products C-MSi with much larger specific surface areas and pore volumes can be obtained after etching i-C-MSi in a 3.0 M NaOH solution. This is due to the dissolution of the unreacted SiO_2 during the hydrothermal process.

FE-SEM images show that the C-SiO_2 possesses a hierarchically porous structure constituted by 3D interconnected carbon walls (Figure S1a, b, Supporting Information online). The micropores and mesopores can also be found in the images. As elucidated by the TEM image (Figure S1c) and the corresponding EDS analysis (Figure S1d), the elements of C, O, N, S, P and Si are present in C-SiO_2. The rose-petal-like structure shown in the FE-SEM images (Figure 1c) indicates that the i-C-CdSi has a large surface area. After etching with NaOH solution, the surface appearance of the C-CdSi (Figure 1d) is similar to the i-C-CdSi, which means that the alkali etching process has little effect on the morphology of the material. Figure 2 displays the TEM images of i-C-CdSi (Figure 2a–d) and C-CdSi (Figure 2e–h), and all of the images exhibit layered rose-petal-like structures. The

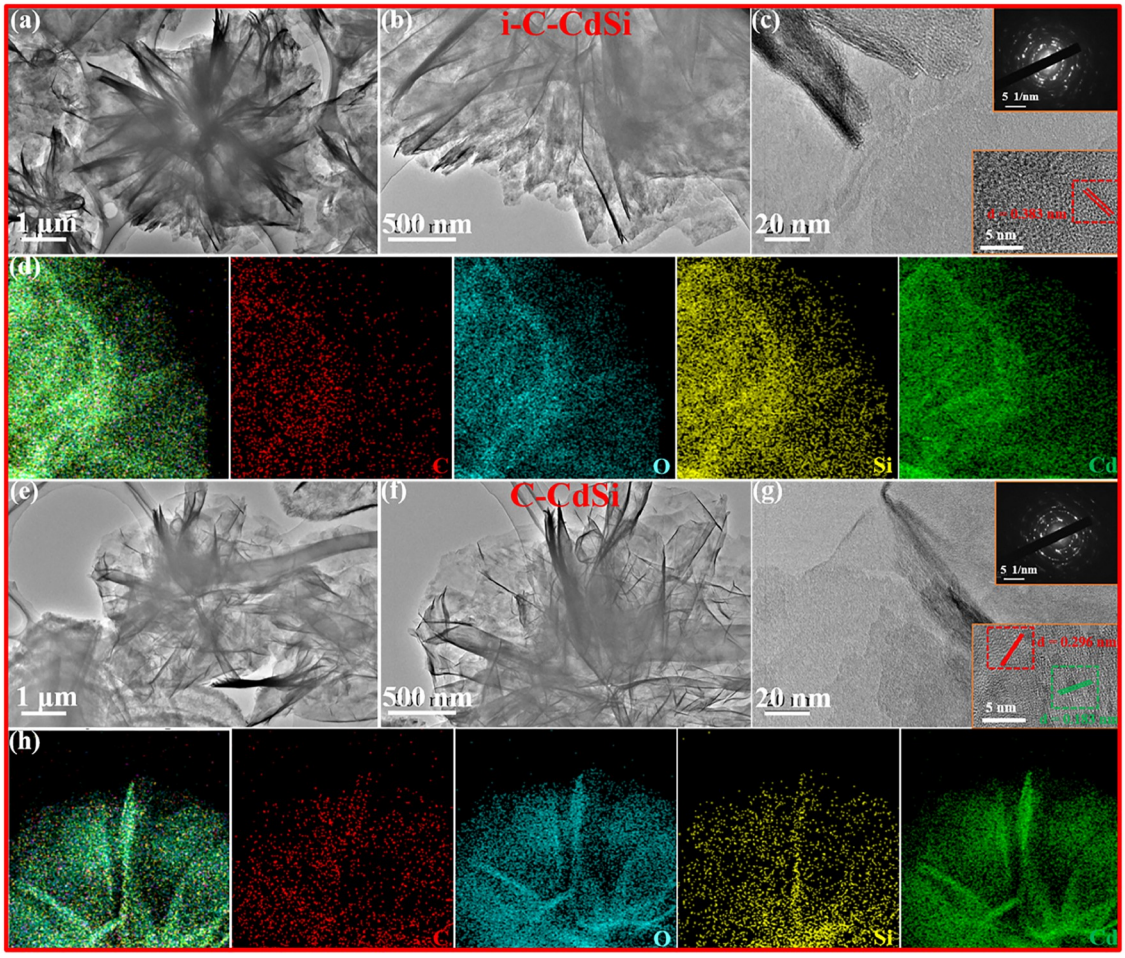

Figure 2 (Color online) TEM images and HAADF images of the i-C-CdSi and C-CdSi: (a–d) i-C-CdSi, (e–h) C-MSi. The inserts in (c, g) are HRTEM and SEAD images.

diffraction rings observed from the SAED images (inset in Figures 2c, g) demonstrate that i-C-CdSi and C-CdSi are polycrystalline structures with low crystallization. The consequence of lattice fringes in the HRTEM images reveals that the spacing of d = 0.383 nm (inset in Figure 2c), and d = 0.296 and 0.183 nm (inset in Figure 2g) belong to the (022) and (040), (153) faces of Cd_2SiO_4 (JCPDS, No. 17-0258) [37]. The EDS mappings of i-C-CdSi (Figure 2d, Figure S2a–d) and C-CdSi (Figure 2h, Figure S2e–h) declare that the content of C, O, Si and Cd accounts for the majority. This indicates that the Cd_2SiO_4 has been formed and evenly distributed on the surface of the carbon framework. A small amount of N, P, S elements were also identified, which come from the GLs. Similarly, Figure 3a–e show the FE-SEM images of C-ZnSi, C-MnSi, C-NiSi, C-CoSi, C-FeSi and C-CuSi with different morphologies. Wherein the morphologies of C-ZnSi, C-MnSi, C-NiSi and C-CoSi are rose-petal-like, while C-FeSi is cube-like and C-CuSi is walnut-like. The results of FE-SEM are consistent with those of TEM characterization. As shown in Figure 3a1–a2, 3b1–b2, 3c1–c2, 3d1–d2, 3e1–e2 and 3f1–f2, the interfringe spacing of d = 0.184, 0.242, 0.148, 0.246, 0.255 and 0.247 (0.234) nm are attributed to the (333), (400), (004), (141), (112), and (111), (111) faces of Zn_2SiO_4 (JCPDS, No. 08-0492), Mn_7SiO_{12} (JCPDS, No. 29-0890), Ni_2SiO_4 (JCPDS, No. 03-0780), Co_2SiO_4 (JCPDS, No. 29-0507), Fe_2SiO_4 (JCPDS, No. 09-0307), and CuO/Cu_2O (JCPDS, No. 03-0892/02-1040), respectively [20,38–42]. According to the mappings inserted in Figure 3a2–f2, the samples exhibit Zn, Mn, Ni, Co, Fe and Cu elements that are uniformly distributed, respectively. This illustrates that ZnSi, MnSi, NiSi, CoSi, FeSi and CuSi have been generated on the surface of the carbon framework. Metal silicates can provide rapid ion transport by shortening diffusion pathways and reducing diffusive resistance to mass transport [43,44]. The conductive carbon layers can serve as paths for fast electron transfer, while the pores can function as active sites for ions [33,45,46]. Thus, the grown metal silicates on the 3D carbon substrate deliver excellent capacitance and high-rate performance of electrodes for the SCs.

Figures S3a and S4 show the XRD patterns of C-SiO_2 and i-C-CdSi-3, while Figure 4a shows the XRD patterns of C-CdSi with various ratios of Cd/Si. No sharp peaks are observed in the XRD pattern of C-SiO_2 (Figure S3a), indicating the amorphous nature of the C-SiO_2. As Cd^{2+} is added during the hydrothermal process, the dispersion peak between 16° and 30° weakens, as shown in Figure S4 and Figure 4a. The appearance of the new peaks at 23.5°, 30.3°, 32.0°, 33.4°, 38.8°, 50.0° and 54.2° in the XRD pattern of i-C-CdSi-3 proves the generation of Cd_2SiO_4 (JCPDS, No. 17-0258) [37]. C-CdSi-3 exhibits almost identical results of XRD pattern with i-C-CdSi-3, proving the little effect of the alkali etching on the structures. The electrochemical performance results, including CV, GCD and EIS by using CHI 660E, manifest that C-CdSi-3 possesses higher properties than those in its corresponding series (C-CdSi-x) and i-C-CdSi-3 (see below). Thus, C-CdSi-3 was selected for further study. For the convenience of narration, in subsequent studies, C-CdSi-3 is simplified as C-CdSi. The XRD patterns of C-ZnSi, C-MnSi, C-NiSi, C-CoSi, C-FeSi and C-CuSi shown in Figure 4d manifest the generation of Zn_2SiO_4 (JCPDS, No. 08-0492), Mn_7SiO_{12} (JCPDS, No. 29-0890), Ni_2SiO_4 (JCPDS, No. 03-0780), Co_2SiO_4 (JCPDS, No. 29-0507), Fe_2SiO_4 (JCPDS, No. 09-0307), and CuO/Cu_2O (JCPDS, No. 03-0892/02-1040) [20,38–42]. This is due to the reaction of M^{2+} and SiO_2 on the surface of amorphous carbon.

The nitrogen adsorption-desorption isotherms and pore size distribution of C-SiO_2 and C-MSi (M = Cd, Zn, Mn, Ni, Co, Fe and Cu) were studied and the corresponding curves are shown in Figure S3 and Figure 4, respectively. Table S1 (Supporting Information online) lists the corresponding BET-specific surface areas and pore volumes. The C-SiO_2 in Figure S3b and C-MSi in Figure 4b, e present types I and IV isotherms, which are often given by microporous and mesoporous carbons [47]. The pore size distribution of C-SiO_2 shown in Figure S3c is mainly in the range of 2–12 nm, that is, mesoporous grade. Moreover, as shown in Table S1, the BET surface area, average pore size, and total pore volume of C-SiO_2 are 317 $m^2\ g^{-1}$, 3.11 nm and 0.36 $cm^3\ g^{-1}$, respectively. After the generation of C-MSi, the BET surface areas are significantly increased compared to C-SiO_2, as well as the average pore sizes and total pore volumes (Figure 4b, c, e, f and Table S1). More specifically, the BET surface areas are 597, 574, 550, 594, 571, 557 and 543 $m^2\ g^{-1}$, the average pore sizes are 3.69, 3.75, 3.49, 3.93, 3.57, 3.19 and 3.31 nm, and the total pore volumes are 0.57, 0.52, 0.51, 0.56, 0.53, 0.50 and 0.49 $cm^3\ g^{-1}$ for C-CdSi, C-ZnSi, C-MnSi, C-NiSi, C-CoSi, C-FeSi and C-CuSi, respectively. These results suggest that the generation of the metal silicates on the surface of the biomass carbon can enlarge the surface area and pore size, thereby providing more active sites for the redox reaction process and promoting the ion insertion during electrochemical charging/discharging [48,49].

Figure S5a shows the FTIR spectra of C-SiO_2 and the C-MSi (M = Cd, Zn, Mn, Ni, Co, Fe and Cu). The peaks at 452 and 1,091 cm^{-1} are assigned to the symmetric and asymmetric stretching modes of Si-O-Si in C-SiO_2, respectively [49]. As for C-CdSi, due to the generation of Cd_2SiO_4, the peak at 1,091 cm^{-1} mostly shifted to 1,051 cm^{-1}. Similarly, the 1,091 cm^{-1} peak shifted to 1,055, 1,058, 1,053, 1,053, 1,055 and 1,055 cm^{-1} after adding Zn^{2+}, Mn^{2+}, Ni^{2+}, Co^{2+}, Fe^{2+}, and Cu^{2+} for the obtain of M-O-Si [19,20,42,50]. For the Raman spectra shown in Figure S5b, all of the materials show two peaks centered around 1,348 and 1,950 cm^{-1}, which correspond to the D-band and the G-band, respectively. The intensity ratio of I_D/I_G is used to analyze the lattice defect and crystallinity of the carbonaceous materials

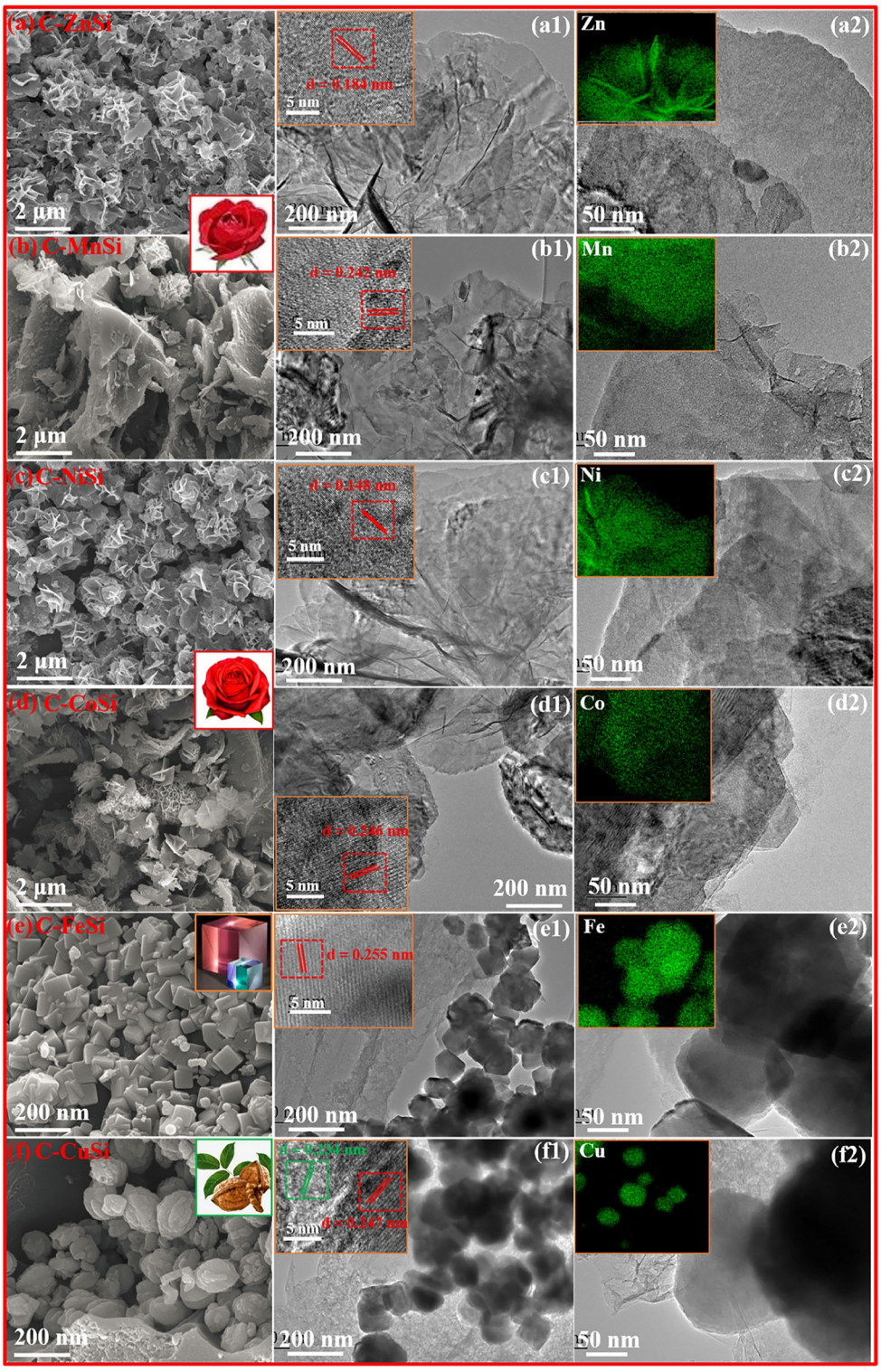

Figure 3 (Color online) FE-SEM images of C-ZnSi (a), C-MnSi (b), C-NiSi (c), C-CoSi (d), C-FeSi (e) and C-CuSi (f); TEM and elemental mapping images of C-ZnSi (a1–a2), C-MnSi (b1–b2), C-NiSi (c1–c2), C-CoSi (d1–d2), C-FeSi (e1–e2) and C-CuSi (f1–f2).

[51]. The I_D/I_G value of C-SiO_2 is calculated to be 0.75. As for C-MSi, the I_D/I_G values are respectively 0.88 (C-CdSi), 0.86 (C-ZnSi), 0.81 (C-MnSi), 0.86 (C-NiSi), 0.84 (C-CoSi), 0.83 (C-FeSi) and 0.81 (C-CuSi), all higher than the value of C-SiO_2, indicating that the formation of metal silicates can produce a large number of defects and vacancies. The creation of defects and vacancies plays a great role in improving electrochemical performance [52].

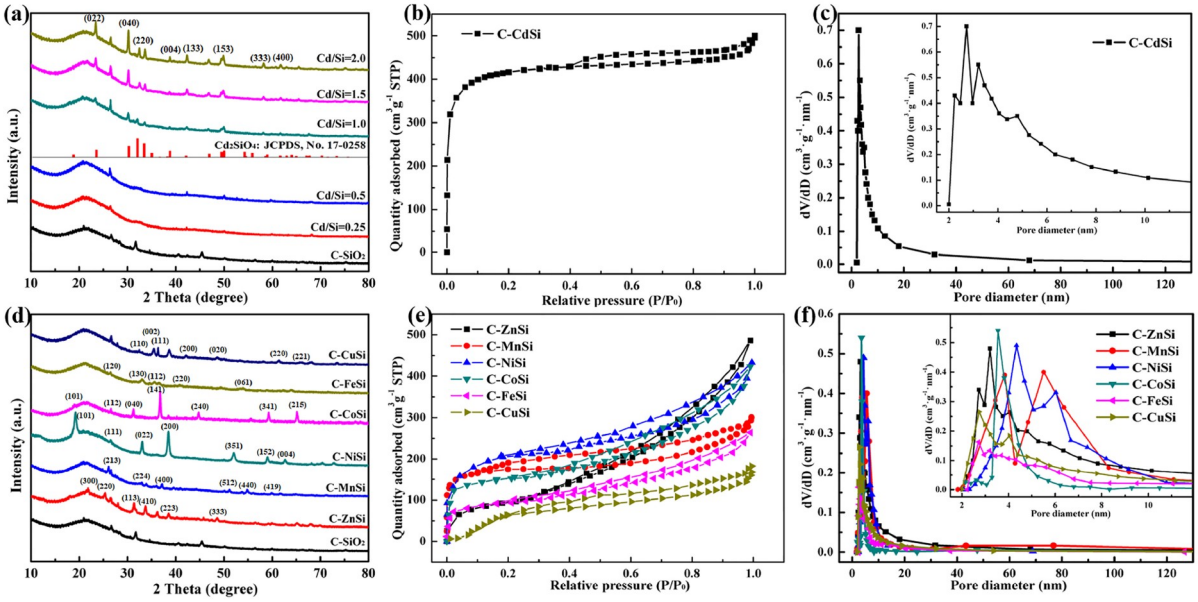

Figure 4 (Color online) (a, d) XRD patterns of C-MSi, (b, e) nitrogen adsorption-desorption isotherms and (c, f) pore size-distribution curves calculated by the BJH method (M = Cd, Zn, Mn, Ni, Co, Fe and Cu).

XPS measurement is carried out to further evaluate the chemical identities of the atoms in the samples. The survey XPS spectra of C-SiO_2 in Figure S6 manifests the existence of C, N, O, Si, P and S elements. Meanwhile, consistent with the result of EDS mappings, pronounced Cd 3d peaks are observed in the survey spectra of C-CdSi in addition to the elements contained in C-SiO_2 (Figure 5 and Figure S7). Paraphrasing, the high-resolution C 1s spectrum (Figure 5a1) is deconvoluted into four peaks: C-N (288.6 eV), C-S-C (286.4 eV), C-C (284.9 eV) and C=C (284.2 eV) [53]. The three peaks in the N 1s spectrum (Figure 5a2) at 405.6, 400.7 and 398.6 eV represent graphitic N, pyrrolic N and pyridinic N, respectively [54]. The O 1s spectrum (Figure 5a3) is fitted by four peaks located at 533.6, 533.1, 532.1 and 531.3 eV, which are assigned to O-N, O-C, O-Si and O-Cd, respectively [55]. The Si 2p spectrum (Figure 5a4) reveals the existence of Cd-O_3Si (102.7 eV), Si-O (102.0 eV) and C-O_3Si (101.5 eV) in C-CdSi [56]. The P 2p spectrum (Figure S7a) displays two peaks: P-O-P (134.5 eV) and P-O-Si (133.0 eV) [51,57]. The four peaks in the S 2p spectrum (Figure S7b) are attributed to S $2p_{3/2}$ (169.3 eV), C=S (168.2 eV), S $2p_{1/2}$ (164.5 eV) and C-SO_x-C (163.7 eV), respectively. The presence of heteroatoms (N, P, S) plays an important role in improving the electrochemical performance of materials. Specifically, the spectrum of Cd 3d (Figure 5a5) shows two individual component peaks at 412.2 and 406.7 eV to Cd $3d_{3/2}$ and Cd $3d_{5/2}$, respectively [58–60]. The XPS spectra of the other C-MSi samples (M = Zn, Mn, Ni, Co, Fe and Cu) are shown in Figure S8 and Figure 5b–g. As for Zn 2p spectrum (Figure 5b), the two peaks at 1,045.9 and 1,023.4 eV representing Zn $2p_{3/2}$ and Zn $2p_{1/2}$, respectively [19,25]. For Mn 2p spectrum (Figure 5c), the peaks at 652.9 and 642.5 eV are assigned to Mn $2p_{3/2}$ and Mn $2p_{1/2}$, respectively [19,50]. The XPS spectrum of Ni 2p (Figure 5d) displays four peaks (882.1, 862.0, 874.2 and 856.0 eV), which ascribed to the shake-up types of Ni $2p_{1/2}$ and Ni $2p_{3/2}$ edge, and Ni $2p_{1/2}$ and Ni $2p_{3/2}$, respectively [20,61]. In the Co 2p spectrum (Figure 5e), the presence of Co $2p_{1/2}$ (797.3 eV), Co $2p_{3/2}$ (782.3 eV) and satellite peaks of Co $2p_{1/2}$ (804.4 eV) and Co $2p_{3/2}$ (787.1 eV) indicates the generation of cobalt-silicate [20,62]. The two peaks shown in the Fe 2p signal (Figure 5f) locked at 724.3 and 711.0 eV are assigned to the Fe $2p_{1/2}$ and Fe $2p_{3/2}$, while the satellite peaks of Fe $2p_{1/2}$ and Fe $2p_{3/2}$ are observed at 727.1 and 712.9 eV, respectively [42,63]. As for Cu 2p spectrum (Figure 5g), the presence of Cu $2p_{1/2}$ (952.7 eV) and Cu $2p_{3/2}$ (932.5 eV) can prove the generation of Cu_2O/CuO [42,64]. Thus, the XPS results show that the energy locations corresponding to C 1s, N 1s, O 1s, Si 2p, P 2p, S 2p and M 2p (M = Cd, Zn, Mn, Ni, Co, Fe and Cu) are basically consistent with those in the previous reports, indicating that these elements coexist in hybridization.

3.2 Electrochemical properties of the electrodes

The metal-silicate samples with the above excellent characteristics must be ideal electrodes for supercapacitors. The electrochemical properties of the materials were evaluated by CV, GCD and EIS measurements using a CHI-660E electrochemical workstation. The measurements were tested in a three-electrode system, and the electrolyte was found to be a 3.0 M KOH solution. The potential windows were chosen *via* CV experiments at 20 mV s^{-1} and as shown in Figure S9, the most suitable potential range should be –1.0 to

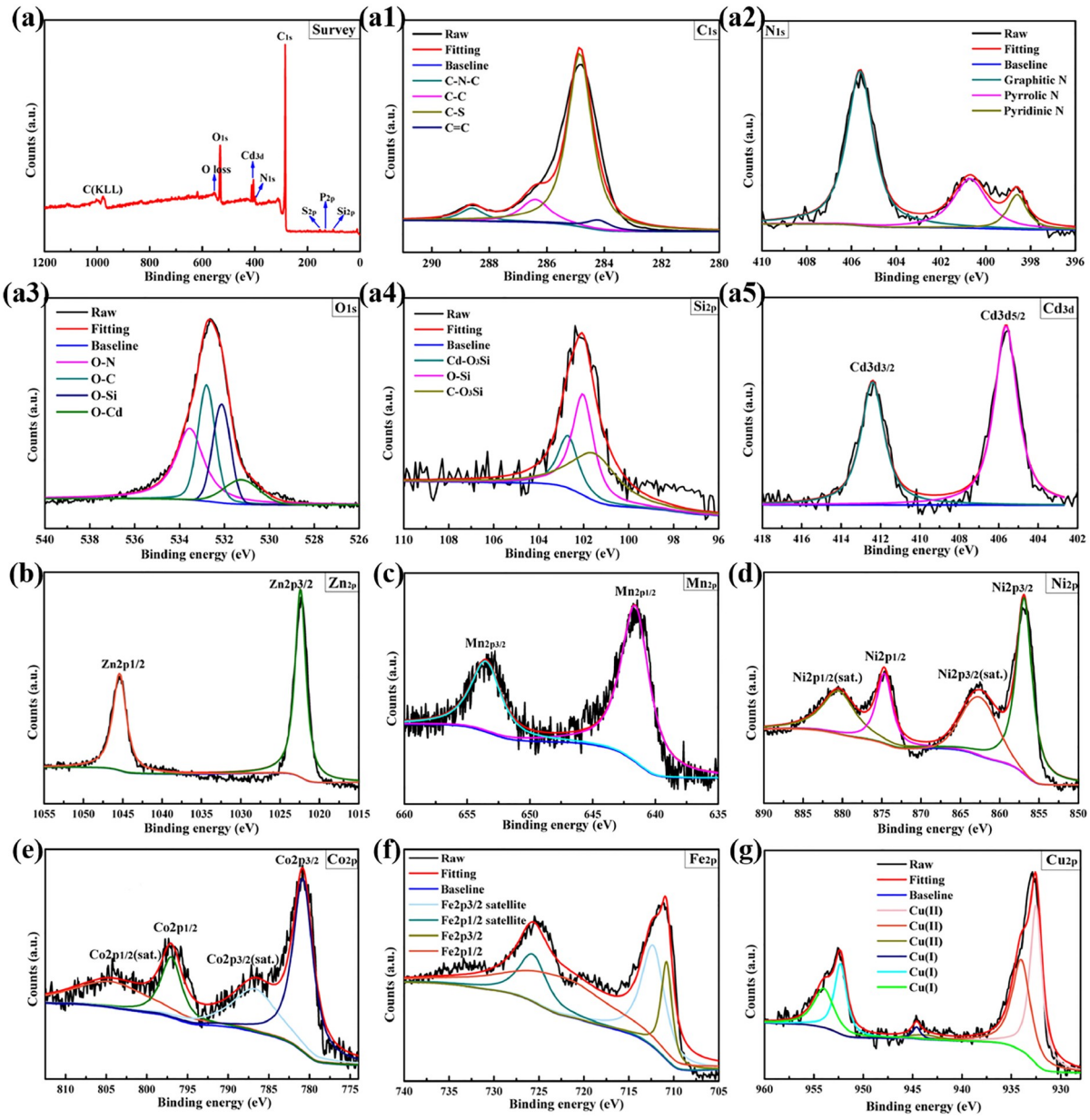

Figure 5 (Color online) XPS spectra of C-CdSi: (a) full spectrum, (a1) C_{1s}, (a2) N_{1s}, (a3) O_{1s}, (a4) Si_{2p}, and (a5) Cd_{3d}. XPS spectra of (b) Zn_{2p}, (c) Mn_{2p}, (d) Ni_{2p}, (e) Co_{2p}, (f) Fe_{2p}, and (g) Cu_{2p}.

0.6 V. The electrochemical performance results, including CV, GCD and EIS of C-SiO_2, i-C-CdSi-3 and C-CdSi-3 were shown in Figures S10 and S11, respectively. Through comparing the electrochemical experiment results, i-C-CdSi-3 and C-CdSi-3 show much better properties than those of C-SiO_2, indicating that the formation of transition metal silicates has a significant improvement in electrochemical performance. Moreover, the etched sample C-CdSi-3 has a larger integral area and longer charge/discharge time than i-C-CdSi-3, declaring the alkali etching process can play a significant role in improving the electrochemical performance of materials. What is more, from the CV and GCD curves of C-CdSi-x (x = 1, 2, 3, 4, and 5) shown in Figure S12 and Figure 6a, b, C-CdSi-3 exhibits the highest electrochemical properties compared with other counterparts (C-CdSi-x, x = 1, 2, 4, and 5). Thus, in the following paper, the electrochemical performance of C-CdSi-3 (donated as C-CdSi) was mainly investigated. Through the CV experiments of the electrodes at different scan rates in the potential range of –1.0 to 0.6 V, the redox reaction in the charging and discharging process were researched and all of the curves exhibit similar shapes. The region from –1.0 to 0.2 V with a rectangular shape is due to the presence of the amorphous carbon electric double-layer capacitance while the field from 0.2 to 0.6 V with a pair of redox peaks is attributed to the existence of the redox capacitance [65–67]. The samples

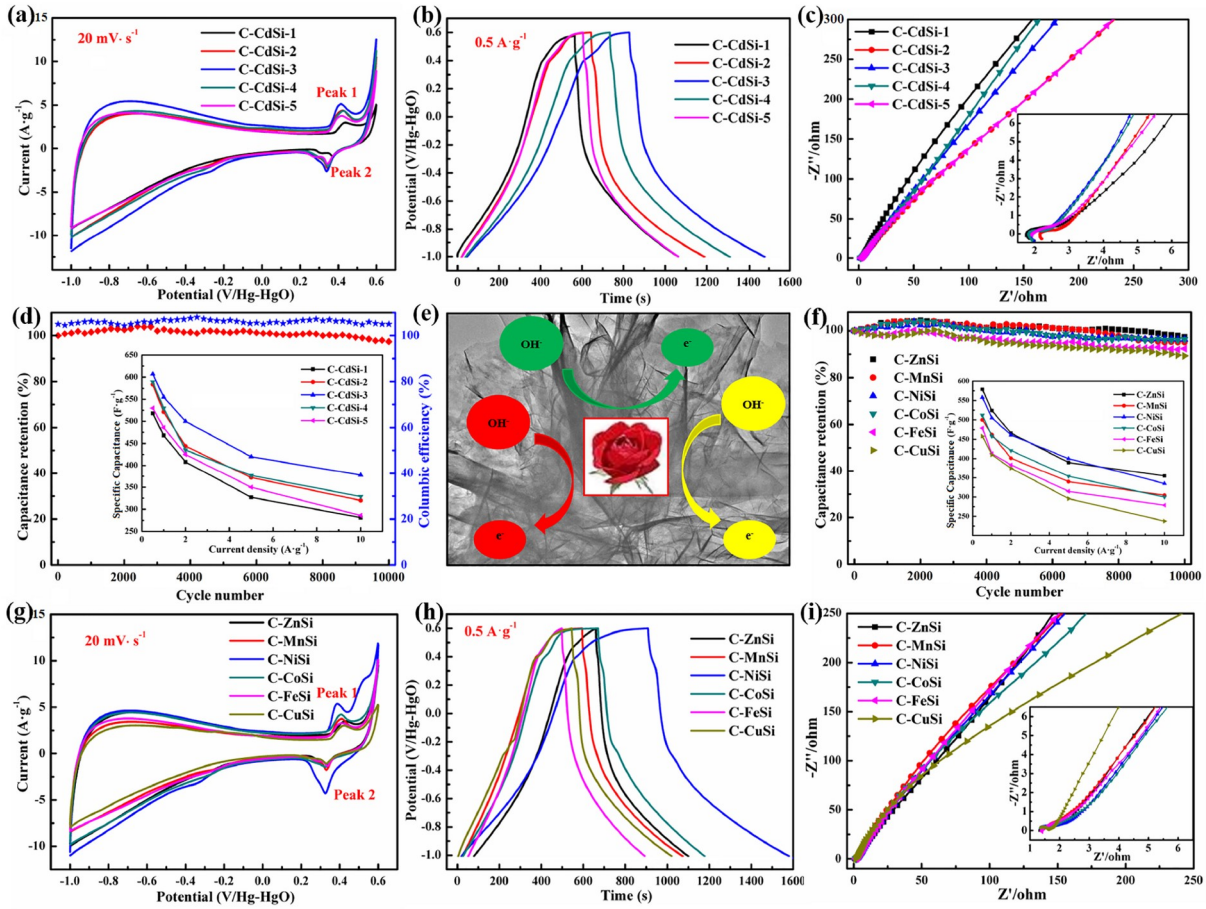

Figure 6 (Color online) (a) CV curves at various ratios of C-CdSi at 20 mV s^{-1}. (b) GCD curves at various ratios of C-CdSi at 0.5 A g^{-1}. (c) Nyquist plots of various ratios of C-CdSi in the frequency range from 100 kHz to 0.01 Hz. (d) Cycling performance and coulombic efficiency of C-CdSi at 1.0 A g^{-1} for 10,000 cycles, the insets are their comparison of the relationship between specific capacitance and current density of C-CdSi. (e) The schematic illustration of the energy storage mechanism on the layered metal silicates. (f) Cycling performance of C-MSi at 1 A g^{-1} for 10,000 cycles, the insets are their comparison of the relationship between specific capacitance and current density of C-MSi. (g) CV curves of C-MSi at 20 mV s^{-1}. (h) GCD curves of C-MSi at 0.5 A g^{-1}. (i) Nyquist plots of C-MSi in the frequency ranging from 100 kHz to 0.01 Hz, (M = Zn, Mn, Ni, Co, Fe and Cu).

maintain their shapes even at high scan rates. This could be ascribed to the large size of pores in the samples, which indicate a fast charge transfer rate and excellent reversible performance.

The potential redox reaction of C-CdSi is as follows:

$$Cd_2^{II}SiO_4 + OH^{\bullet-} \leftrightarrow Cd_2^{III}SiO_4(OH)^{\bullet-} + e^{\bullet-}$$

Similarly, the CV and GCD curves of C-ZnSi, C-MnSi, C-NiSi, C-CoSi, C-FeSi and C-CuSi are shown in Figures S13 and S14 and Figure 7a, b. The reaction mechanism of C-ZnSi [19], C-MnSi [19], C-NiSi [20], C-CoSi [20] and C-FeSi [42] can be summarized in the following equations, respectively:

$$Zn_2^{II}SiO_4 + OH^{\bullet-} \leftrightarrow Zn_2^{III}SiO_4(OH)^{\bullet-} + e^{\bullet-}$$
$$Mn_7^{II}SiO_{12} + OH^{\bullet-} \leftrightarrow Mn_7^{III}SiO_{12}(OH)^{\bullet-} + e^{\bullet-}$$
$$Ni_2^{II}SiO_4 + OH^{\bullet-} \leftrightarrow Ni_2^{III}SiO_4(OH)^{\bullet-} + e^{\bullet-}$$
$$Co_2^{II}SiO_4 + OH^{\bullet-} \leftrightarrow Co_2^{III}SiO_4(OH)^{\bullet-} + e^{\bullet-}$$
$$Fe_2^{II}SiO_4 + OH^{\bullet-} \leftrightarrow Fe_2^{III}SiO_4(OH)^{\bullet-} + e^{\bullet-}$$

As for C-CuSi, the redox reaction can be summarized as a quasi-reversible conversion [42,61,68]:

$$2CuO + H_2O + 2e^{\bullet-} \leftrightarrow Cu_2O + 2OH^{\bullet-}$$
$$Cu_2O + H_2O + 2OH^{\bullet-} \leftrightarrow 2Cu(OH)_2 + 2e^{\bullet-}$$
$$CuOH + OH^{\bullet-} \leftrightarrow CuO + H_2O + e^{\bullet-}$$
$$CuOH + OH^{\bullet-} \leftrightarrow Cu(OH)_2 + e^{\bullet-}$$

The Nyquist plots of the electrodes were tested by EIS measurement that can investigate their kinetics. From Figure S11c and Figure 6c, i, at the high-frequency region and low-frequency region, all of the curves are composed of semi-circles and straight lines, respectively. The shape of the curve has a significant impact on the performance of the electrode; that is, the resistance of the electrode is affected by the size of the semicircle, while the diffusion rate of the electrolyte ions is based on the slope of the straight line [69]. Thus, as shown in Figure 6c, C-CdSi-3 possesses a larger slope than the other C-CdSi-*x* (x = 1, 2, 4, and 5) and i-C-CdSi-3, indicating that the diffusion and migration of ions can be accelerated by the alkali etching process.

The specific capacitance of the electrodes is displayed in Figure 6d (C-CdSi-*x*, x = 1, 2, 3, 4, 5) and Figure 6f (C-MSi,

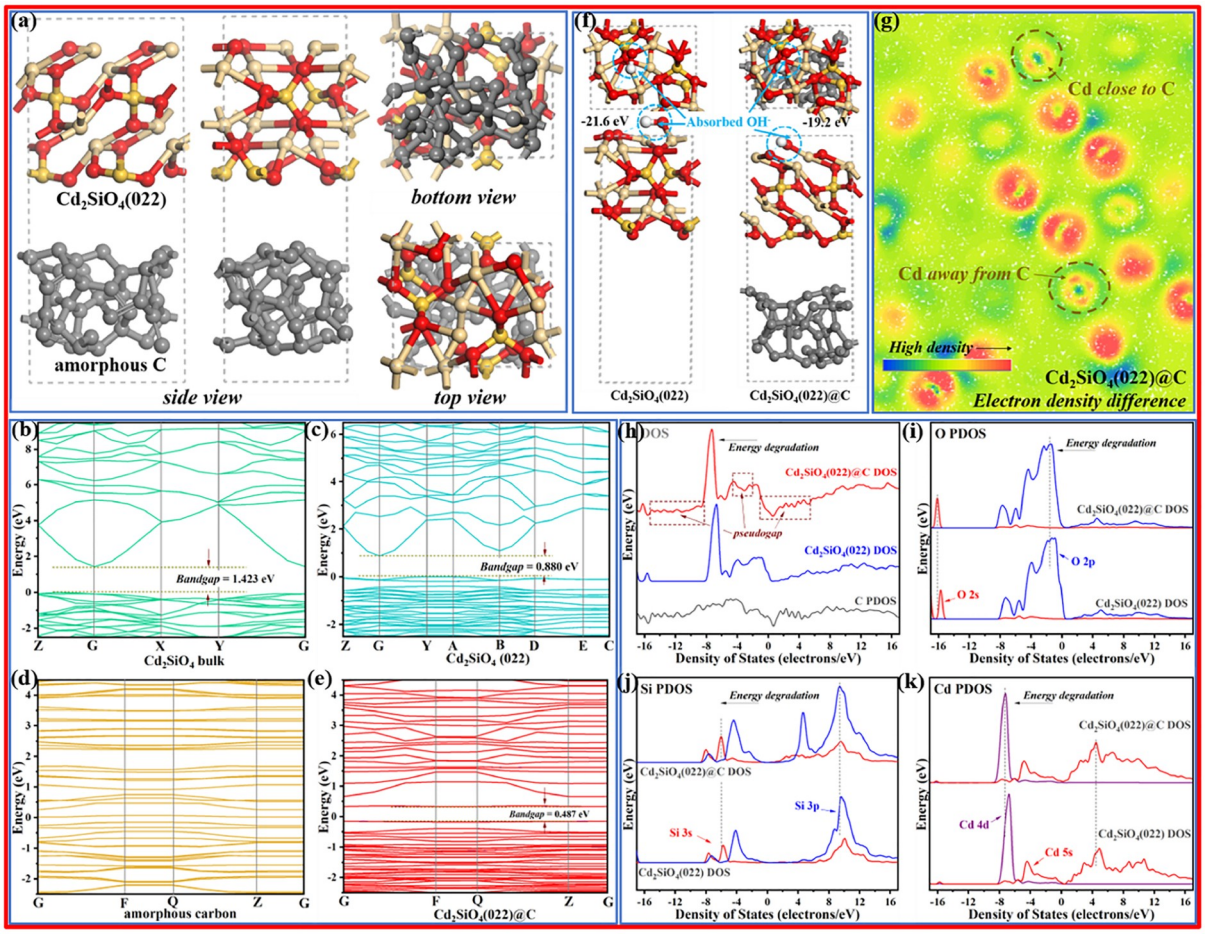

Figure 7 (Color online) (a) The crystalline structure of $Cd_2SiO_4(022)$@C. Band structures of (b) Cd_2SiO_4 bulk, (c) Cd_2SiO_4 (022), (d) amorphous carbon and (e) $Cd_2SiO_4(022)$@C. (f) Adsorption energies and the corresponding models of $OH^{\bullet-}$ on $Cd_2SiO_4(022)$ and $Cd_2SiO_4(022)$@C. (g) Electron density difference of $Cd_2SiO_4(022)$@C. (h) Density of states of amorphous carbon, $Cd_2SiO_4(022)$ and $Cd_2SiO_4(022)$@C. Partial density of states of (i) O, (j) Si and (k) Cd in Cd_2SiO_4 (022) and $Cd_2SiO_4(022)$@C, respectively.

M = Zn, Mn, Ni, Co, Fe and Cu), respectively. At a current density of 0.5 A g^{-1}, the high specific capacitance (for a single electrode) of C-CdSi-3 reaches 607 F g^{-1}. Moreover, the C-CdSi-3 still retains high values at the high current density of 1.0, 2.0, 5.0 and 10.0 A g^{-1}, respectively. The values are much higher than those of other C-CdSi-*x* electrodes (*x* = 1, 2, 4, 5). As for the other C-MSi electrodes shown in Figure 6f, the values are 579 (C-ZnSi), 500 (C-MnSi), 558 (C-NiSi), 512 (C-CoSi), 479 (C-FeSi) and 458 (C-CuSi) F g^{-1} at 0.5 A g^{-1}, respectively. It can be seen from the results of CV, GCD, EIS and specific capacitance the electrochemical performance can be enhanced by the treatment with NaOH. As the entry of the electrolyte into active materials and the penetration rate of electrons can be improved by increasing the surface areas and multilayer structures, the alkali etching process is an efficient way to improve the electrochemical performance [21,70]. What is more, as for the C-MSi (M = Cd, Zn, Mn, Ni, Co, Fe and Cu), in addition to their own properties, the morphology of materials may have a greater impact on their electrochemical properties. For example, the electrochemical performance of rose-like C-CdSi is better than the cube-like C-FeSi and the walnut-like C-CuSi, which may be partly due to the larger surface area and structure of the rose-like morphology of the C-CdSi. Compared with other silicate-based electrodes, as shown in Table S2, the C-MSi electrodes obtained from gourd leaves show preferable electrochemical performance.

The electrochemical kinetic behavior of the samples is studied and analyzed by CV curves with an increasing scan rate, as shown in Figure S15. The relationship between redox peaks' current and sweep rate can be defined by the following laws:

$$i = av^b$$

$$\log i = \log a + b\log v$$

where the *a* and *b* are variable parameters and the value *b* ranges from 0.5 to 1, which is equal to the slope of log(*i*) and log(*v*) plots. The capacity can be mainly attributed to the diffusion-controlled behavior when *b* is close to 0.5 while related to the surface-control when *b* is close to 1. The *b*-values of the samples are all close to 1, demonstrating that

they mainly exhibit surface-controlled behavior [21,22]. In detail, the *b*-values of C-MSi (M = Cd, Zn, Mn, Ni, Co, Fe and Cu) are respectively equal to 0.97, 0.95, 0.89, 0.92, 0.91, 0.87 and 0.85.

The cycling stability and columbic efficiency of C-CdSi are explored by the GCD test at 1.0 A g^{-1}. As shown in Figure 6d, the cycle life test conducted reveals that C-CdSi also shows long-term cycling stability with 98.2% of the initial capacitance retention after 10,000 cycles. In particular, due to the electro-activation of the electrode, the capacitance reaches its maximum after about 2,350 cycles [71,72]. The corresponding columbic efficiency of C-CdSi is 108.4%. After 10,000 cycles, the capacitances of C-ZnSi, C-MnSi, C-NiSi, C-CoSi, C-FeSi and C-CuSi maintain 97.4%, 95.1%, 96.4%, 96.3%, 92.4% and 89.3%, respectively (Figure 6f). The excellent cycling performance results of these materials prove that the metal silicates grown on the calcined amorphous carbon from gourd leaves can maintain operational stability as an electrode material. Table S2 also lists the reusable performance of some other electrode materials based on silicate. It can be seen that the metal silicates discussed in this study exhibit more significant electrochemical performance.

3.3 Theoretical analysis

To further understand the mechanism behind the excellent capacitance, DFT calculations were performed.

The structures of geometrically optimized amorphous carbon, Cd_2SiO_4(022) and Cd_2SiO_4(022)@C, are shown in Figure S16 and Figure 7a, respectively. The energy of Cd_2SiO_4(022)@C is –26,047.53 eV, which is lower than the sum of amorphous carbon (–6,574.24 eV) and Cd_2SiO_4(022) (–19,446.45 eV) at –26,040.69 eV, indicating that the combination of amorphous carbon and Cd_2SiO_4(022) is stable [73]. The DFT calculations are also employed to analyze the electronic conductivity [74]. The calculated bandgap of Cd_2SiO_4 is about 1.423 eV (Figure 7b), indicating that it is almost an electronic insulator. The calculated bandgap of Cd_2SiO_4(022) is about 0.880 eV (Figure 7d), while the Cd_2SiO_4(022)@C is about 0.487 eV (Figure 7f). The bandgap decreased with the introduction of amorphous carbon on Cd_2SiO_4(022), demonstrating the enhanced electroconductibility of CdSi@C. Moreover, bands of Cd_2SiO_4(022)@C flatten significantly, meaning a decreasing interaction between the atoms and increasing effective quality of current carriers, which are conducive to electron conduction. The density of states (DOS) and partial density of states (PDOS) were performed for amorphous carbon, Cd_2SiO_4(022) and Cd_2SiO_4(022)@C, to elucidate the contribution of different atomic orbitals, especially in amorphous carbon [75]. As shown in Figure 7h, after composite with amorphous carbon, the overall electronic state of Cd_2SiO_4(022)@C shifts towards lower energy levels, proving the enhanced stability of the material [76]. Noteworthily, the addition of the electronic state of amorphous carbon leads to more narrow pseudo-energy gaps in the DOS diagram, corresponding to the flatter band shape in the energy band diagram. From the PDOS calculation in Figure 7i–k, after composite with carbon materials, the overall electronic state shifts towards lower energy levels, proving the enhanced stability of the material. The corresponding electron density difference of Cd_2SiO_4(022)@C (Figure 7g) depicts that Cd atoms approach to carbon atoms exhibits lower electron density compared with that of Cd atoms farther away from carbon atoms. This phenomenon originates from the II Electronic supplement of amorphous carbon to atomic orbitals of Cd_2SiO_4, indicating that the electrophilicity of Cd active sites is weakened, facilitating insertion and removal of adsorption of OH^- for energy storage. The above results prove that amorphous carbon in CdSi@C not only conducts electricity itself but also acts as an electron supply for the increasing conductivity and energy storage performance of CdSi [77]. According to the results of adsorption energy, OH^- occupies the Cd_2SiO_4(022) plane with the lowest energy and shows the highest probability. Therefore, the (022) plane is calculated for the electronic structures of Cd_2SiO_4(022) and Cd_2SiO_4(022)@C. As shown in Figure 7f, the adsorption energy towards OH^- for Cd_2SiO_4 (022) and Cd_2SiO_4(022)@C is –21.6 and –19.2 eV, respectively, meaning that it is easier for Cd_2SiO_4(022)@C to insertion and removal of OH^- for completing rapid surface redox reactions and higher pseudo-capacitance [78].

Similarly, DFT calculations were also applied to several other materials such as C-MnSi (Mn_7SiO_{12}(400)@C), C-NiSi (Ni_2SiO_4(004)@C) and C-CuSi (Cu_2O(111)@CuO(111)@C). The calculation results are shown in Figures S17–S19. The corresponding electron density difference of Mn_7SiO_{12}(400)@C (Figure S17b), Ni_2SiO_4(004)@C (Figure S18b) and Cu_2O(111)@CuO(111)@C (Figure S19b) describe that compared to Mn, Ni, and Cu atoms further away from carbon atoms, these atoms closer to carbon atoms exhibit lower electron density. The calculated bandgap of Mn_7SiO_{12}(400)@C (Figure S17c–e), Ni_2SiO_4(004)@C (Figure S18c–e) and Cu_2O(111)@CuO(111)@C (Figure S19c–h) is about 0, 0.14 and 0 eV, respectively. These data are much smaller than amorphous carbon or Mn_7SiO_{12}(400), Ni_2SiO_4(004) and Cu_2O(111)@CuO(111), indicating that the enhanced electroconductibility with the combination of amorphous carbon and these metal compounds. The lower energy levels and more narrow pseudo energy gaps in the DOS diagrams of Mn_7SiO_{12}(400)@C, Ni_2SiO_4(004)@C and Cu_2O(111)@CuO(111)@C shown in Figures S17f, S18f and S19i proved that the combination process is beneficial for improving the stability of the materials.

Therefore, supercapacitor electrodes with C-MSi (M = Cd,

Zn, Mn, Ni, Co, Fe and Cu) coating would ultimately show satisfactory overall electrochemical performance, and the calculation results complement the experimental results perfectly.

3.4 Electrochemical performance of metal silicates as hybrid supercapacitor devices

In order to explore the practical applications of the metal silicates obtained from gourd leaves, for example, to explain why the Calabash Brothers are invincible in the story, the flexible solid-state hybrid supercapacitor devices (HSCs) were fabricated. In this study, the HSCs were composed of C-MSi (M = Cd, Zn, Mn, Ni, Co, Fe and Cu) as positive electrodes and AC as negative electrodes. The HSCs are denoted as C-MSi//AC. The measurements were tested in a two-electrode system using a CHI-660E electrochemical workstation. The electrolyte is 3.0 M PVA/KOH.

It can be seen from the various operating voltage ranges of the C-CdSi//AC device shown in Figure S20 that 0–1.5 V is the most suitable window. Figure 8a displays the CV curves of the C-CdSi//AC device, and even at high scan rates, the device still maintains a roughly rectangular shape. This can be ascribed to the enlarged size of pores in the C-CdSi using NaOH, which indicates excellent rate capabilities of the C-CdSi//AC device [79]. As shown in Figure 8b, the charge/discharge of the GCD curves exhibits approximate symmetry. This suggests that the C-CdSi//AC device has ideal capacitive behavior [80,81]. The Nyquist plot curve of the C-CdSi//AC device tested by EIS is shown in Figure 8c, which is composed of a straight line at the low-frequency region and a semicircle at the high-frequency region [82,83]. The steepest linear curve in the low-frequency region means a splendid capacitive performance [34].

The areal capacitances of the C-CdSi//AC device derived from the GCD curves are shown in Figure 8d. The capacitance decreases from 691 to 444 mF cm^{-2} with the current density increase from 2 to 10 mA cm^{-2}, still offers a high specific capacitance even at 10 mA cm^{-2} (64.3% capacitance retention), suggesting good rate capacity. The superb rate capacity can benefit from the short diffusion distance and the low ion transport resistance during the charge/discharge process. Furthermore, the corresponding energy density shown in inset of Figure 8e also decreases from 5.04 to 3.8 Wh m^{-2}, corresponding to the power density increases from 22.2 to 99.8 W m^{-2}. The trends of energy density and power density are opposite, proving that there is a great potential of using these electrode materials to prepare the SCs with high efficiency [56]. C-CdSi//AC device also shows a high stability of 87.3% after 6,000 cycles, which is investigated by the GCD test at a current density of 1.0 A g^{-1} (Figure 8f). The columbic efficiency is about 105% at every cycle, demonstrating that the C-CdSi//AC device has reliable capacitive performance during the charge/discharge process.

As for the other C-MSi//AC devices (M = Zn, Mn, Ni, Co, Fe and Cu), the CV, GCD and Nyquist plot curves are shown in Figure 8g–i, respectively. The appropriate operating voltage windows of C-MSi//AC devices are 0–1.6 V (C-ZnSi//AC, C-NiSi//AC and C-CoSi//AC), 0–1.4 V (C-MnSi//AC and C-CuSi//AC), and 0–1.2 V (C-FeSi//AC), respectively. The CV, GCD and Nyquist plot curves indicate the C-MSi//AC devices reveal excellent electrochemical performance: excellent rate capabilities, splendid capacitive behavior and outstanding electrical conductivity. The areal capacitance versus current density of C-MSi//AC is shown in Figure 8j. The specific capacitances are 684 (C-ZnSi//AC), 607 (C-MnSi//AC), 660 (C-NiSi//AC), 618 (C-CoSi//AC), 576 (C-FeSi//AC) and 549 (C-CuSi//AC) mF cm^{-2} at the current density of 2 mA cm^{-2}, respectively. The energy density *versus* power density of C-MSi//AC are shown in Figure 8k. The energy densities are 5.11, 4.48, 4.80, 4.35, 4.51 and 4.15 Wh m^{-2} at the power density of 21.1, 16.7, 19.6, 18.7, 15.8 and 14.8 W m^{-2}, respectively. Figure 8l demonstrates the C-MSi//AC devices maintain high stability after 6,000 cycles (86.3%, 83.8%, 85.4%, 85.0%, 82.1% and 81.3% of their initial capacitance values of C-ZnSi//AC, C-MnSi//AC, C-NiSi//AC, C-CoSi//AC, C-FeSi//AC and C-CuSi//AC, respectively). Table S3 summarizes all electrochemical performance results of the C-MSi//AC devices and compared with most other SC devices in previous literatures, the HSC devices in this research exhibit significant electrochemical properties.

3.5 Further extended to prepare metal silicates using other diverse biomass-derived carbon materials from the gourds

We further synthesized the metal silicates using other parts from the gourds using the same strategy. Five hierarchically porous heteroatom-doped carbon materials derived from the roots, vines, flowers, fruits and seeds of gourds are prepared and Figure 9a–e are their photographs of precursors. Then a certain amount of $Cd(OAc)_2 \cdot 2H_2O$ react with these materials at 180 °C for 24 h, respectively. FE-SEM and TEM images confirm that the obtained carbon samples possess hierarchically porous architectures while the obtained metal silicates possess different morphologies (Figure 9a1–e1 and Figure 9a2–e2). The N_2 sorption analysis verifies the existence of mesoporous and microporous in each sample and the pore sizes are generally distributed between 2–10 nm (Figure 9a3–e3 and Figure 9a4–e4). Their pore structure information is listed in Table S4. The XRD patterns shown in Figure 9a5–e5 prove the generation of Cd_2SiO_4 with varying crystallinity (JCPDS, No. 17-0258). The five materials are also used as electrodes and SCs to further confirm the versatility of this strategy (Figure 9f1–f5 and Figure 9g1–g5)

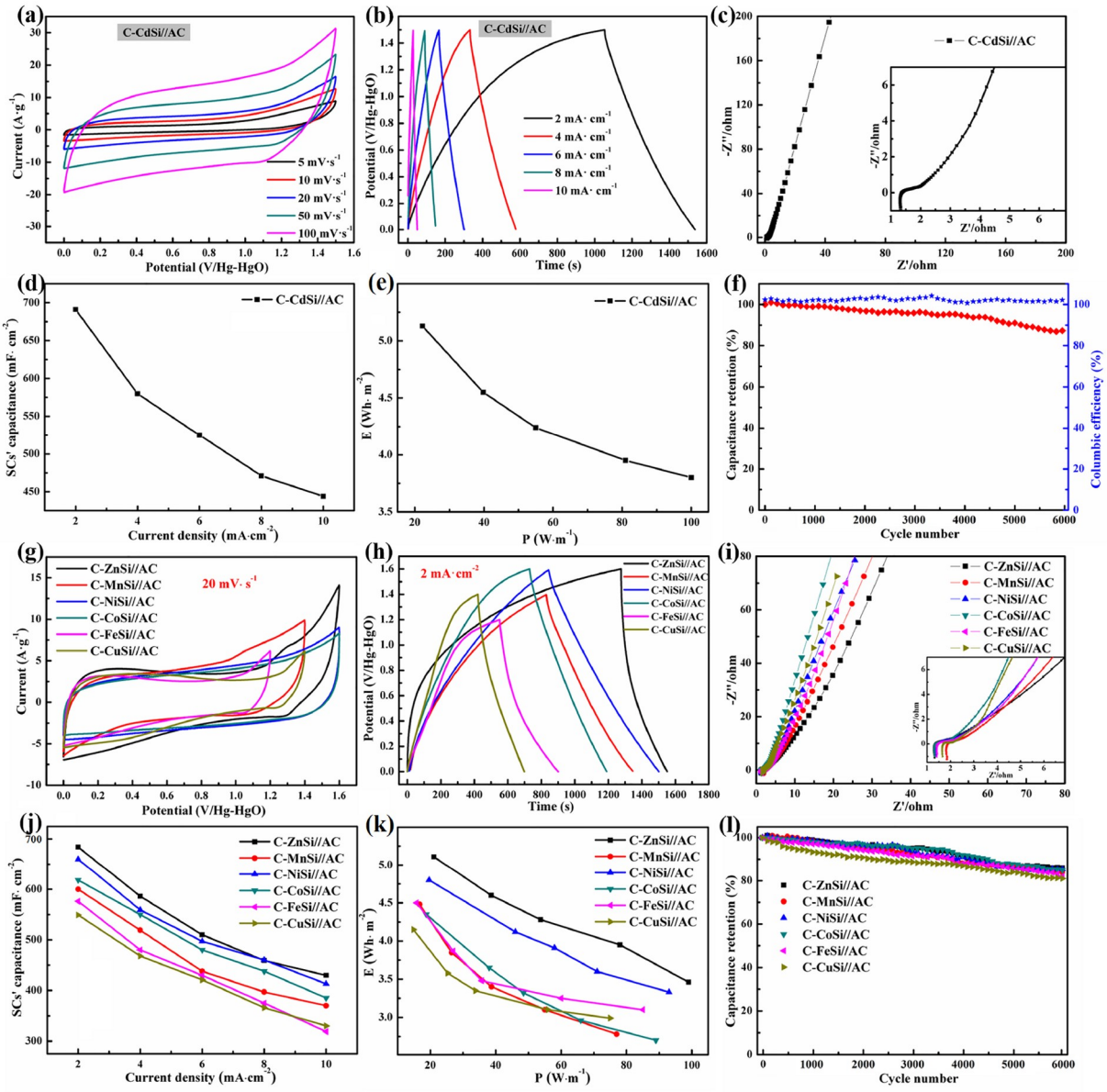

Figure 8 (Color online) (a) CV curves of C-CdSi//AC device at various scan rates from 5 to 100 mV s^{-1}. (b) GCD curves of C-CdSi//AC device at various current densities from 2 to 10 mA cm^{-2}. (c) Nyquist plots of C-CdSi//AC device, in the frequency ranging from 100 kHz to 0.01 Hz. (d) Capacitance of C-Cd/Si at different scan rates. (e) The Ragone plot. (f) Cycling performance and coulombic efficiency for 6,000 cycles. (g) CV curves of C-MSi//AC devices at 20 mV s^{-1}. (h) GCD curves of C-MSi//AC devices at 2 mA cm^{-2}. (i) Nyquist plots of C-MSi//AC devices, in the frequency ranging from 100 kHz to 0.01 Hz. (j) Capacitance of C-MSi//AC at different scan rates. (k) Ragone plots. (l) Cycling performance of the assembled devices at 20 mV s^{-1} for 6,000 cycles (M = Zn, Mn, Ni, Co, Fe and Cu).

and their electrochemical performance results are listed in Tables S5 and S6. By comparison, supercapacitors made from gourd leaves perform better than those of roots, vines, flowers, fruits, and seeds.

The above results prove C-MSi (M = Cd, Zn, Mn, Ni, Co, Fe and Cu) as a promising material for advanced electrodes for electrochemical supercapacitors. The unique hierarchical porous structures, the high S_{BET}, and the heteroatom-doped carbon of the C-MSi lead to their extraordinarily large and stable energy storage performance. Other than those, they also have the following three advantageous multiple co-operative effects.

(1) The nanostructures can shorten the ions' transport length, while the meso-/micropores on the surface of nanostructures can supply a fast transfer rate and adequate mass transport for ions.

(2) The super high S_{BET} provides an appropriate electrode/electrolyte interface to facilitate fast charge transfer and charge capacity.

(3) The performance can be enhanced to an exceptional level by heteroatom-doping, which is due to the enhancement of defect sites, electrochemical reactivity, and electro-

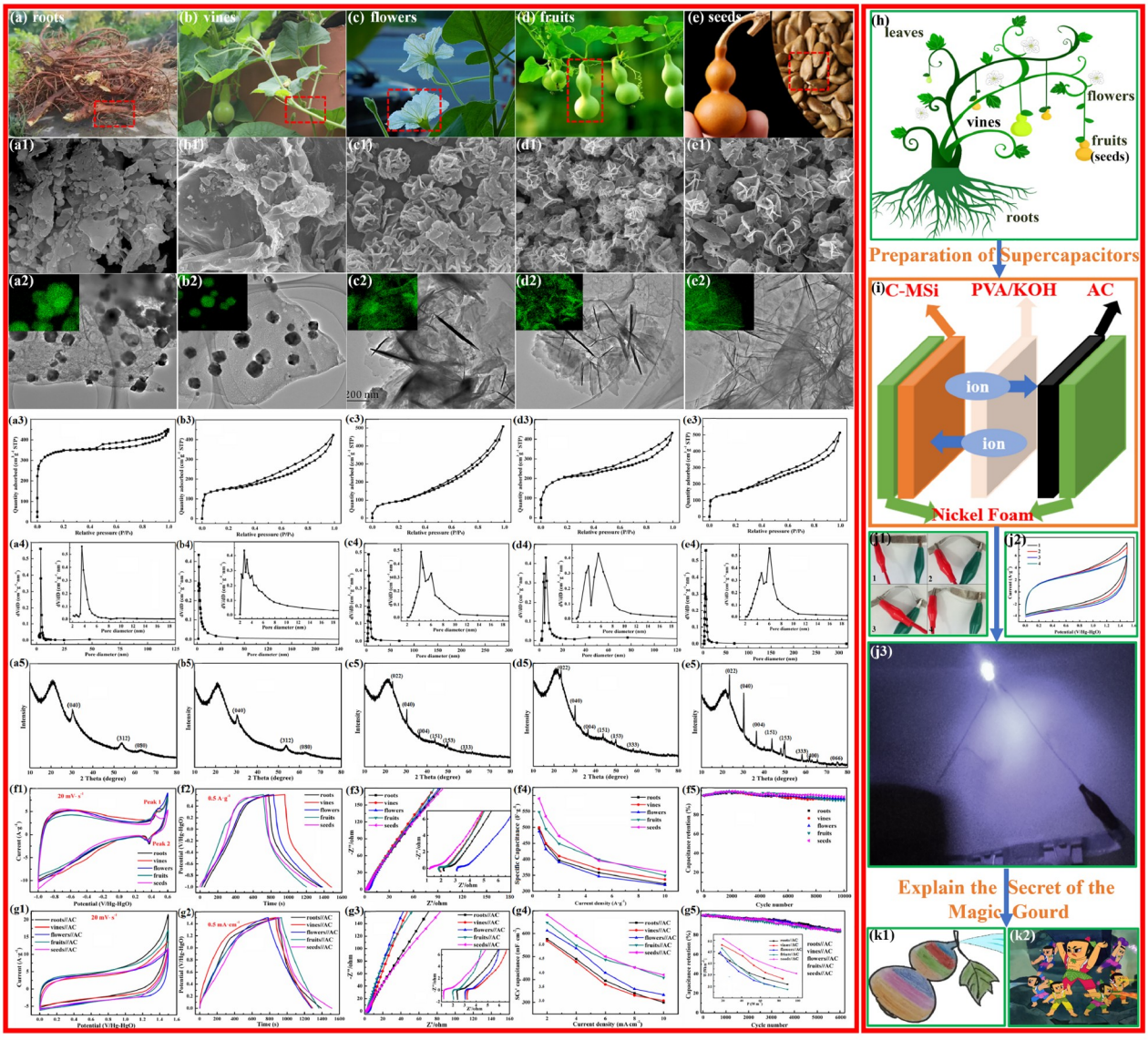

Figure 9 (Color online) (a–e) Photographs of different biomass precursors from the gourd: (a) roots, (b) vines, (c) flowers, (d) fruits, and (e) seeds. (a1–e1) FE-SEM images, (a2–e2) TEM images, (a3–e3) nitrogen adsorption-desorption isotherms, (a4–e4) pore size-distribution curves calculated by the BJH method, and (a5–e5) XRD patterns of the C-CdSi from the roots, vines, flowers, fruits and seeds, respectively. (f1–f5) Electrochemical performance of the C-CdSi electrodes from the roots, vines, flowers, fruits and seeds, respectively. (g1–g5) Electrochemical performance of the C-CdSi//AC hybrid supercapacitor devices from the roots, vines, flowers, fruits and seeds, respectively. (h–k) Explanation of the secret of the magic gourd.

nic conductivity.

The above elements have excellent multiple cooperative effects, that is, interaction and easy transportation to improve the electrochemical performance of electrode materials.

Thus, the mechanism of supercapacitors that used transition metal silicates grown on the amorphous carbon as positive electrodes (Figure 9h–k) may explain the secret of the magic gourd: The supercapacitors manufactured by calabash brothers using various parts of the gourd plants have excellent electrochemical performance, such as excellent capacitance and cycling stability, playing a role in energy storage and conversion in generating energy and defeating powerful enemies.

4 Conclusions

In order to decrypt the secret of the magic gourd, natural gourd leaves (GLs) were used to synthesize metal silicates. Then, the C-MSi (M = Cd, Zn, Mn, Ni, Co, Fe and Cu) materials were used to fabricate supercapacitor electrodes and devices. By integrating theoretical calculations and experimental results, the supercapacitor electrodes and devices obtained from the combination of transition metals with amorphous carbon exhibit superior electrochemical performance. This is due to the high specific surface area and layered porous structure of the metal silicates anchored on the biomass carbon, which can shorten the paths to transfer

electrons and ions. This approach is very versatile and was also applied to produce many hierarchically structured metal-silicate materials of other biomass precursors, including roots, vines, flowers, fruits and seeds of the planted gourds. Thus, the secret of the magic gourd can be explained by using gourd plants as raw materials to prepare the supercapacitors with excellent electrochemical performance. The research results of this paper also provide a novel and potential way to prepare new metal silicates from other biomaterials for the enhancement of electrochemical performance and improvement of energy storage and conversion.

Acknowledgements This work was supported by the Horizontal Project from the Dalian Wonful Pharmaceutical Co., Ltd (881150), the Anhui Province Applied Peak Cultivation Discipline (XK-XJGF005), the Anhui Province Quartz Sand Purification and Photovoltaic Glass Engineering Research Center ([2022]547-49), the Natural Science Foundation of Anhui Province (KJ2020A0055) and the National Natural Science Foundation of China (21771030). The authors also acknowledge the assistance of the DUT (Dalian University of Technology) Instrumental Analysis Center.

Conflict of interest The authors declare no conflict of interest.

Supporting information The supporting information is available online at http://chem.scichina.com and http://link.springer.com/journal/11426. The supporting materials are published as submitted, without typesetting or editing. The responsibility for scientific accuracy and content remains entirely with the authors.

1 Zhang J. Chinese snake woman resurfaces in comics: Considering the case study of calabash brothers. In: *Monstrous Women in Comics*. Oxford: University Press of Mississippi, 2020. 207
2 Li X, Guan BY, Gao S, Lou XWD. *Energy Environ Sci*, 2019, 12: 648–655
3 Guan BY, Yu L, Lou XWD. *J Am Chem Soc*, 2016, 138: 11306–11311
4 Liu Y, Pan Z, Tian D, Hu T, Jiang H, Yang J, Sun J, Zheng J, Meng C, Zhang Y. *Chem Eng J*, 2020, 399: 125842
5 Yuan M, Guo X, Liu Y, Pang H. *J Mater Chem A*, 2019, 7: 22123–22147
6 Schüth F. *Angew Chem Int Ed*, 2003, 42: 3604–3622
7 Owusu KA, Qu L, Li J, Wang Z, Zhao K, Yang C, Hercule KM, Lin C, Shi C, Wei Q, Zhou L, Mai L. *Nat Commun*, 2017, 8: 14264
8 Shao Y, El-Kady MF, Sun J, Li Y, Zhang Q, Zhu M, Wang H, Dunn B, Kaner RB. *Chem Rev*, 2018, 118: 9233–9280
9 Dong X, Jing X, Mu Y, Yu Y, Miao C, Meng C, Huang C, Zhang Y. *Chem Eng J*, 2021, 431: 133277
10 Lai F, Miao YE, Zuo L, Lu H, Huang Y, Liu T. *Small*, 2016, 12: 3235–3244
11 Zhang Y, Liu S, Zheng X, Wang X, Xu Y, Tang H, Kang F, Yang QH, Luo J. *Adv Funct Mater*, 2016, 27: 1604687
12 Wu ZY, Liang HW, Chen LF, Hu BC, Yu SH. *Acc Chem Res*, 2016, 49: 96–105
13 Chen Q, Tan X, Liu Y, Liu S, Li M, Gu Y, Zhang P, Ye S, Yang Z, Yang Y. *J Mater Chem A*, 2020, 8: 5773–5811
14 Chen C, Huang Y, Zhu Y, Zhang Z, Guang Z, Meng Z, Liu P. *ACS Sustain Chem Eng*, 2020, 8: 1497–1506
15 Jin C, Nai J, Sheng O, Yuan H, Zhang W, Tao X, Lou XWD. *Energy Environ Sci*, 2021, 14: 1326–1379
16 Matsagar BM, Yang RX, Dutta S, Ok YS, Wu KCW. *J Mater Chem A*, 2021, 9: 3703–3728
17 Kwon HJ, Hwang JY, Shin HJ, Jeong MG, Chung KY, Sun YK, Jung HG. *Nano Lett*, 2020, 20: 625–635
18 Zeng J, Dong L, Sun L, Wang W, Zhou Y, Wei L, Guo X. *Nano-Micro Lett*, 2021, 13: 373–386
19 Zhang S, Zheng J, Wei J, Zhang Y, Niu F, Wang Y, Yan H, Li Z, Meng C. *J Colloid Interface Sci*, 2022, 623: 135–145
20 Zhang S, Yan H, Wang Y, Niu F, Guo T, Zhang Y, Li Z, Wang X, Meng C. *J Anal Appl Pyrolysis*, 2022, 167: 105687
21 Zhang Y, Wang C, Dong X, Jiang H, Hu T, Meng C, Huang C. *Chem Eng J*, 2021, 417: 127964
22 Zhang Y, Jiang H, Wang Q, Meng C. *Chem Eng J*, 2018, 352: 519–529
23 Cheng J, Yan H, Lu Y, Qiu K, Hou X, Xu J, Han L, Liu X, Kim JK, Luo Y. *J Mater Chem A*, 2015, 3: 9769–9776
24 Zeng J, Wei L, Guo X. *J Mater Chem A*, 2017, 5: 25282–25292
25 Zhang S, Liu Y, Zheng J, Mu Y, Jiang H, Yan H, Wang Y, Zhang Y, Meng C. *Dalton Trans*, 2021, 50: 9438–9449
26 Zhang S, Cui M, Zhang Y, Li Z, Meng C. *Mater Chem Front*, 2022, 6: 2447–2457
27 Wang D, Li F, Yin L, Lu X, Chen Z, Gentle IR, Lu GQM, Cheng H. *Chem Eur J*, 2012, 18: 5345–5351
28 Zhao J, Zhang Y, Wang T, Li P, Wei C, Pang H. *Adv Mater Inter*, 2015, 2: 1400377
29 Oraon R, De Adhikari A, Tiwari SK, Nayak GC. *ACS Sustain Chem Eng*, 2016, 4: 1392–1403
30 Long W, Fang B, Ignaszak A, Wu Z, Wang YJ, Wilkinson D. *Chem Soc Rev*, 2017, 46: 7176–7190
31 Wang YY, Hou BH, Lü HY, Wan F, Wang J, Wu XL. *RSC Adv*, 2015, 5: 97427–97434
32 Caballero A, Hernán L, Morales J. *ChemSusChem*, 2011, 4: 658–663
33 Stephan AM, Kumar TP, Ramesh R, Thomas S, Jeong SK, Nahm KS. *Mater Sci Eng-A*, 2006, 430: 132–137
34 Qiu C, Ai L, Jiang J. *ACS Sustain Chem Eng*, 2018, 6: 4492–4498
35 Yao Y, Wu F. *Nano Energy*, 2015, 17: 91–103
36 Zhao J, Zheng M, Run Z, Xia J, Sun M, Pang H. *J Power Sources*, 2015, 285: 385–392
37 Tang C, Zhu J, Wei X, He L, Zhao K, Xu C, Zhou L, Wang B, Sheng J, Mai L. *Energy Storage Mater*, 2017, 7: 152–156
38 Ning K, Zhao G, Liu H, Hu M, Huang F, Li H, Zhang L, Zhu G, Wang H, Shi J. *Diamond Relat Mater*, 2022, 126: 109080
39 Nzabahimana J, Liu Z, Guo S, Wang L, Hu X. *ChemSusChem*, 2020, 13: 1923–1946
40 Liu J, Kopold P, van Aken PA, Maier J, Yu Y. *Angew Chem*, 2015, 127: 9768–9772
41 Liu J, Sun X, Song P, Zhang Y, Xing W, Xu W. *Adv Mater*, 2013, 25: 6879–6883
42 Zhou J, Lian J, Hou L, Zhang J, Gou H, Xia M, Zhao Y, Strobel TA, Tao L, Gao F. *Nat Commun*, 2015, 6: 8503
43 Li J, Liu K, Gao X, Yao B, Huo K, Cheng Y, Cheng X, Chen D, Wang B, Sun W, Ding D, Liu M, Huang L. *ACS Appl Mater Interfaces*, 2015, 7: 24622–24628
44 Li X, Wei J, Li Q, Zheng S, Xu Y, Du P, Chen C, Zhao J, Xue H, Xu Q, Pang H. *Adv Funct Mater*, 2018, 28: 1800886
45 Kumar T, Rai PK, Rai AK, Rai NK, Rai AK, Parigger CG, Watal G, Yadav S. *Foundations*, 2022, 2: 981–998
46 Chen H, Shang S, Tian L, Zhu G. *Chin J Trop Crop*, 2021, 42: 1572
47 Hou J, Cao C, Idrees F, Ma X. *ACS Nano*, 2015, 9: 2556–2564
48 Feng H, Hu H, Dong H, Xiao Y, Cai Y, Lei B, Liu Y, Zheng M. *J Power Sources*, 2016, 302: 164–173
49 Wu X, Jiang L, Long C, Fan Z. *Nano Energy*, 2015, 13: 527–536
50 Qie L, Chen W, Xu H, Xiong X, Jiang Y, Zou F, Hu X, Xin Y, Zhang Z, Huang Y. *Energy Environ Sci*, 2013, 6: 2497–2504
51 Masjedi-Arani M, Salavati-Niasari M. *Ultrasons SonoChem*, 2018, 43: 136–145
52 Zaid MHM, Matori KA, Yaakob Y, Alibe IM. *Optics Laser Tech*, 2021, 140: 106991
53 Si J, Zhao G, Lan T, Ni J, Sun W, Liu Y, Lu Y. *ACS Catal*, 2022, 13:

1033–1044
54 Zhang S, Zhu N, Mao F, Zhang J, Huang X, Li F, Li X, Wu P, Dang Z. *J Hazard Mater*, 2021, 402: 123791
55 Jiang D, Xue J, Wu L, Zhou W, Zhang Y, Li X. *Appl Catal B-Environ*, 2017, 211: 199–204
56 Zhang S, Zhang T, Dong B, Chen J, Meng C. *J Colloid Interface Sci*, 2023, 630: 11–20
57 Lopa NS, Akbari MK, Wu D, Verpoort F, Zhuiykov S. *Energy Fuels*, 2023, 37: 3142–3151
58 Qie L, Chen WM, Wang ZH, Shao QG, Li X, Yuan LX, Hu XL, Zhang WX, Huang YH. *Adv Mater*, 2012, 24: 2047–2050
59 Hu C, Wang L, Zhao Y, Ye M, Chen Q, Feng Z, Qu L. *Nanoscale*, 2014, 6: 8002–8009
60 Li X, Tang Y, Song J, Yang W, Wang M, Zhu C, Zhao W, Zheng J, Lin Y. *Carbon*, 2017, 129: 236–244
61 Li X, Ding S, Xiao X, Shao J, Wei J, Pang H, Yu Y. *J Mater Chem A*, 2017, 5: 12774–12781
62 Wang Q, Zhang Y, Jiang H, Li X, Cheng Y, Meng C. *Chem Eng J*, 2019, 362: 818–829
63 Pallavolu MR, Vallem S, Nallapureddy RR, Adem S, Joo SW. *ACS Appl Energy Mater*, 2023, 6: 812–821
64 Lu W, Yang Y, Zhang T, Ma L, Luo X, Huang C, Ning J, Zhong Y, Hu Y. *J Colloid Interface Sci*, 2021, 590: 226–237
65 Xiang J, Zhu R, Chen Q, Lv G, Yang Y. *Appl Clay Sci*, 2022, 221: 106464
66 Zhang Y, Wang C, Jiang H, Wang Q, Zheng J, Meng C. *Chem Eng J*, 2019, 375: 121938
67 Zhang Y, Jiang H, Wang Q, Zheng J, Meng C. *Appl Surf Sci*, 2018, 447: 876–885
68 Wu M, Liu B, Li J, Su X, Liu W, Li X. *Environ Sci Pollut Res*, 2023, 30: 12608–12617
69 Kannan AG, Choudhury NR, Dutta NK. *Polymer*, 2007, 48: 7078–7086
70 Al Hattali OA, Al Marzouqi F, Al Mamari S, Kuvarega AT, Selvaraj R. *Inorg Chem Commun*, 2022, 146: 110071
71 Birben NC, Paganini MC, Calza P, Bekbolet M. *Photochem Photobiol Sci*, 2017, 16: 24–30
72 Yao X, Jawad BahrAluloom Y, Farhan Jawad S, Hafdhi Abdtawfeeq T, Rahman Al-janabi D, Ahmad N, Alshehri AM, Hadrawi SK, Mohammed Al-Taee M, Riadi Y, Jushi Janani B, Fakhri A. *J Photochem Photobiol A-Chem*, 2023, 436: 114374
73 Shao P, Tian J, Duan X, Yang Y, Shi W, Luo X, Cui F, Luo S, Wang S. *Chem Eng J*, 2019, 359: 79–87
74 Guo P, Wang C. *RSC Adv*, 2017, 7: 4437–4443
75 Yin M, Wu CK, Lou Y, Burda C, Koberstein JT, Zhu Y, O′Brien S. *J Am Chem Soc*, 2005, 127: 9506–9511
76 Rong Q, Long LL, Zhang X, Huang YX, Yu HQ. *Appl Energy*, 2015, 153: 63–69
77 Wang J, Nie P, Ding B, Dong S, Hao X, Dou H, Zhang X. *J Mater Chem A*, 2017, 5: 2411–2428
78 Gao X, Zhao Y, Dai K, Wang J, Zhang B, Shen X. *Chem Eng J*, 2019, 384: 123373
79 Pendashteh A, Mousavi MF, Rahmanifar MS. *Electrochim Acta*, 2013, 88: 347–357
80 Yar A, Dennis J, Mohamed N, Mian M, Irshad M, Mumtaz A. *AIP Conf Proc*, 2016, 1787: 050002
81 Zhang Y, Chen M, Hu T, Meng C. *ACS Appl Nano Mater*, 2019, 2: 2934–2945
82 Wang G, Lu X, Ling Y, Zhai T, Wang H, Tong Y, Li Y. *ACS Nano*, 2012, 6: 10296–10302
83 Zheng J, Zhang Y, Meng C, Wang X, Liu C, Bo M, Pei X, Wei Y, Lv T, Cao G. *Electrochim Acta*, 2019, 318: 635–643